JOURNAL OF COMPUTATIONAL PHYSICS **124,** 351–367 (1996)
ARTICLE NO. 0065

Direct Numerical Simulation of Flow Past Elliptic Cylinders

R. MITTAL AND S. BALACHANDAR

Department of Theoretical and Applied Mechanics, University of Illinois at Urbana-Champaign, Urbana, Illinois 61801

Received April 28, 1994; revised May 17, 1995

Flow over elliptic cylinders can be considered prototypical of flow over a range of bluff bodies since the geometry allows one to study the effect of both thickness and angle-of-attack on the flow field. Therefore, a careful study of this flow should provide valuable insight into the phenomenon of unsteady separation and the structure of bluff body wakes. With this in mind, a spectral collocation technique has been developed to simulate the full three-dimensional incompressible flow over elliptic cylinders and, unlike spectral element and spectral multidomain techniques, here the flow is solved in a single domain. The equations are discretized on a body-fitted elliptic cylindrical grid and properties of the metric associated with this coordinate system are used to solve the governing equations in an efficient manner. Key issues including the inflow and outflow boundary conditions and time-discretization are discussed in detail with the hope that this will facilitate future simulations of similar flows. Finally, we present results of two- and three-dimensional simulations for a range of flow and geometric parameters. The results are compared with available experimental data and it is found that important quantities like Strouhal numbers and drag coefficients match well with established values.

INTRODUCTION

The phenomenon of flow separation and bluff body wakes has long been intensely studied because of its fundamental significance in flow physics and its practical importance in aerodynamic and hydrodynamic applications. Flow behind a circular cylinder has become the canonical problem for studying such external separated flows [1–3]. Engineering applications, on the other hand, often involve flows over complex bodies like wings, submarines, missiles, and rotor blades, which can hardly be modelled as a flow over a circular cylinder. In such flows, parameters such as thickness ratio and angle-of-attack can greatly influence the nature of separation and the wake structure. A fundamental study of flow over a complex non-canonical object would therefore significantly augment our current understanding of wake flows.

There are, however, practical reasons why separating flows over complex shapes do not lend themselves easily to analytical, experimental, or numerical treatment. Due to the complicated nature of the flow, theoretical analysis is typically limited to either flows at very low Reynolds number [4] or flows at early times after an impulsive start [5]. Experimental techniques have become very sophisticated in recent years but an extensive spatial and temporal analysis of the three-dimensional (3D) flow field would quickly overwhelm the available resources. Numerical simulations provide a promising approach to analyzing this problem. However, there remain a number of issues that need to be addressed, namely intelligent grid generation, efficient solution of the governing equations, and the ability to interpret the gigabytes of data that would be generated from the simulations.

Here we consider elliptic cylinders which are more general geometrical configurations than the canonical circular cylinder and provide a richer flow behavior characteristic of typical engineering flow configurations. For these cylinders, changes in eccentricity allow for shapes ranging from that of a circular cylinder to a flat plate. There have been a few numerical simulations of flows over elliptic cylinders. Notable among these are those by Lugt and Haussling [6, 7] and Blodgett [8]. Lugt and Haussling have studied the flow over thin ellipses at various angles-of-attack for low Reynolds numbers [6] and also the details of start-up over elliptic cylinders at 45° angle-of-attack [7]. Blodgett [8] has performed a systematic study of two-dimensional (2D) flow over cylinders with various eccentricities and angles-of-attack at Reynolds number ranging up to 1000. The above studies are limited to 2D simulations and are based on the vorticity-streamfunction formulation of the Navier–Stokes equations.

In the past decade, direct numerical simulation of 3D flows at low to moderate Reynolds number have become possible and have primarily utilized spectral methods for spatial discretization. Spectral methods provide exponential accuracy through their global approximation [9] but their application has been generally limited to simple geometries. Spectral element [10] and spectral multidomain [11] methods have been developed to handle problems in complex geometries and have become quite popular in recent years. These methods provide great flexibility in handling a broad range of geometric configurations but are computationally expensive and relatively difficult to implement. For the relatively simpler class of geometries like elliptic cylinders, prolate/oblate spheroids, and Juo-

0021-9991/96 $18.00

kowski airfoils, more specialized spectral methods based on a single domain and body-fitted orthogonal grid would be expected to perform efficiently and are the method of choice. The justification for developing efficient but specialized methods for these shapes come from recognizing the fact that these shapes encompass a wide range of configurations which are of practical as well as fundamental importance.

This paper describes the simulation of 3D incompressible flow over elliptic cylinders using a Fourier–Chebyshev spectral collocation method in a single domain. The governing equations are written in a body-fitted elliptic cylindrical coordinate system. Special properties of the metric associated with this curvilinear coordinate system are used to develop an efficient direct-solution methodology for the Helmholtz equations arising from the momentum equations and the pressure Poisson equation. This methodology can be extended to other geometries such as prolate and oblate spheroids and bipolar coordinates.

In the present simulations, a technique similar to the buffer-domain technique of Streett and Macareg [11] and the viscous sponge technique of Karniadakis and Triantafyllou [1] is used to handle the specification of outflow boundary conditions. The main difference is that their techniques are implemented in conjunction with multidomains (or multiple elements), whereas the current methodology is based on a single domain. It is demonstrated through extensive tests that this boundary condition allows large vortical disturbances to convect out of the domain without any reflections. To allow for the displacement effect of the boundary layer to be felt in the inflow portion of the outer boundary, a novel mixed boundary condition has also been implemented which improves the behavior of solution at the inflow–outflow junction. Time-split methods [12, 13], despite inherent splitting errors [14–17], are used widely in computational fluid dynamics [1, 11, 18, 19]. In this paper we outline a method based on an influence matrix technique [20, 21] for the removal of errors associated with the imposition of ad-hoc boundary conditions for a two-step time-split scheme.

A number of test cases have been simulated and both 2D and 3D results are presented. The geometrical and flow parameters are chosen to provide a good representation of the full parameter space. Quantities like drag coefficients and Strouhal numbers are compared with existing experimental results in order to validate the current simulation methodology.

SIMULATION METHODOLOGY

Coordinate System and Governing Equations

Elliptic cylindrical coordinates are made up of confocal ellipses and hyperbolas and form an orthogonal system. The mapping between Cartesian (x, y, z) and elliptic (ξ, η, z) coordinates is given by

$$x = a\cosh\xi\cos\eta; \quad y = a\sinh\xi\sin\eta; \quad z = z, \tag{1}$$

where a is the distance between the center and the foci of the ellipse. Furthermore, lines of constant ξ correspond to confocal ellipses and lines of constant η to hyperbolas. The elliptic coordinate system introduces the following metrics in the three mutually orthogonal directions

$$h_\xi = h_\eta = h = a\sqrt{\sinh^2\xi + \sin^2\eta}; \quad h_z = 1. \tag{2}$$

The governing equations of the flow are the incompressible Navier–Stokes equations which in the elliptic coordinate system take the form:

$$\text{Continuity,} \qquad \frac{1}{h^2}\frac{\partial(hu)}{\partial\xi} + \frac{1}{h^2}\frac{\partial(hv)}{\partial\eta} + \frac{\partial w}{\partial z} = 0 \tag{3}$$

$$\text{Momentum conservation,} \quad \frac{\partial\mathbf{u}}{\partial t} + \mathbf{NL}(\mathbf{u}) = -\nabla P + \frac{1}{\mathrm{Re}}\mathbf{D}(\mathbf{u}), \tag{4}$$

where (u, v, w) are the contravariant velocity components along the (ξ, η, z) directions, respectively, and $\mathbf{NL}(\mathbf{u})$ and $\mathbf{D}(\mathbf{u})$ are the non-linear advection and diffusion terms, respectively. The above equations have been non-dimensionalized using the semi-major axis (L_x) of the ellipse as the length scale and the freestream velocity (U_∞) as the velocity scale. The Reynolds number is thus given by $\mathrm{Re} = L_x U_\infty/\nu$, where ν is the kinematic viscosity. The other important parameters are the three dimensionless geometric quantities: thickness ratio ($\mathscr{T}$), angle-of-attack (α) and spanwise aspect ratio (A). The thickness ratio of the ellipse is given by $\mathscr{T} = L_y/L_x$, where L_y is the length of the semi-minor axis, and the spanwise aspect ratio by $A = L_z/L_x$, where L_z is the spanwise length of the elliptic cylinder.

Spatial Discretization

A Fourier–Chebyshev collocation scheme is used for the spatial discretization of the governing equations. A Chebyshev expansion is used in the wall normal (ξ) direction and the Gauss–Lobatto collocation points are computed as

$$\xi_i = \frac{1}{2}\cos\left[\frac{\pi(i-1)}{(N_\xi - 1)}\right](\xi_E - \xi_O) + \frac{1}{2}(\xi_E + \xi_O) \quad \text{for } i = 1, 2, ..., N_\xi, \tag{5}$$

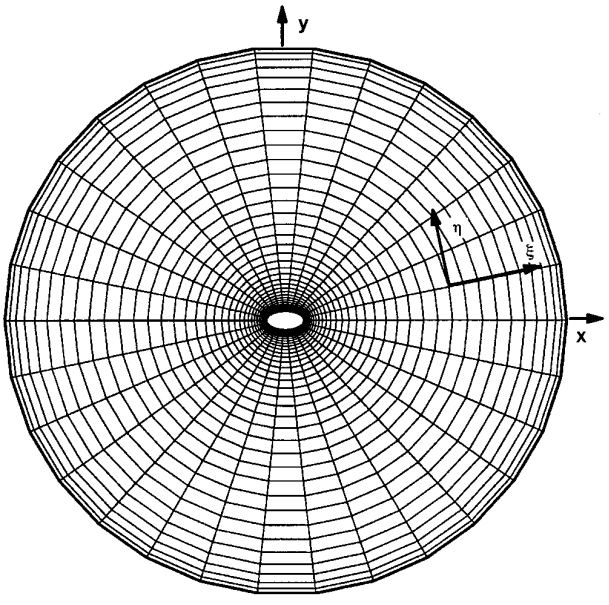

FIG. 1. A representative 2D computational grid. Actual grids are significantly finer than this grid.

where ξ_E represents the elliptic cylinder, ξ_O represents the ellipse which forms the outer limit of the computational domain, and N_ξ is the number of grid points in the wall normal direction. ξ_E and ξ_O can be computed in terms of the thickness ratio as $\xi_E = \frac{1}{2} \ln [(1 + \mathscr{T})/(1 - \mathscr{T})]$ and $\xi_O = \ln[x_O \cosh \xi_E + \sqrt{x_O^2 \cosh^2 \xi_E - 1}]$, where x_O is the distance of the imaginary outer ellipse measured along the abscissa. Also, the distance between the center and the foci of the ellipse is given by $a = (\cosh \xi_E)^{-1}$.

The azimuthal direction (η) is intrinsically periodic with period 2π and a Fourier expansion is employed along this direction. The collocation points along this direction are thus computed as $\eta_j = 2\pi(j - 1)/N_\eta$ for $j = 1, 2, ..., N_\eta$, where N_η is the number of grid points in this direction. Also, the flow is considered to be periodic along the spanwise direction with period L_Z and therefore a Fourier expansion is also employed along z. Here spanwise periodicity is used as a model for flow over a cylinder with infinite spanwise extent. Over the range of Reynolds numbers ($180 \lesssim \mathrm{Re} \lesssim 1000$) considered in this study, it is known from experiments [3] that the wake is dominated by structures which have a well-defined periodic structure in the spanwise direction. Thus, imposition of periodicity in the spanwise direction, coupled with an appropriately chosen spanwise length, should ensure faithful reproduction of the important physics of the flow field. The collocation points along the z direction are therefore uniformly distributed and are given by $z_k = A(k - 1)/N_z$ for $k = 1, 2, ..., N_z$, where N_z is the number of grid points in the spanwise direction. A representative 2D grid is shown in Fig. 1.

Temporal Discretization

A time-split method has been used to advance the solution in time. This method relies on the idea of operator splitting to uncouple the pressure computation from that of the velocity field and provides an efficient method for solving the incompressible Navier–Stokes equations. The typical two-step version of the time-split method advances the solution from time level "n" to "$n + 1$" through an intermediate level. In the present simulations, the first step is the advection-diffusion step and it proceeds as

$$\frac{\mathbf{u}^* - \mathbf{u}^n}{\Delta t} + \mathbf{NL}(\mathbf{u}^n) = \frac{1}{\mathrm{Re}} \mathbf{D}(\mathbf{u}^*) \quad \text{in } \Omega \tag{6}$$

$$\mathbf{u}^* = \mathbf{u}_E \quad \text{on } \partial\Omega_E \tag{7}$$

$$\mathbf{B}(\mathbf{u}^*) = 0 \quad \text{on } \partial\Omega_O, \tag{8}$$

where Ω refers to the interior of the computational domain and $\partial\Omega_E$ and $\partial\Omega_O$ refer to the cylinder surface and outer boundary, respectively. Details of the boundary conditions (7) and (8) will be given in a later section. The advection-diffusion step is followed by the pressure correction step,

$$\frac{\mathbf{u}^{n+1} - \mathbf{u}^*}{\Delta t} = -\nabla P^{n+1} \quad \text{in } \Omega \tag{9}$$

$$\nabla \cdot \mathbf{u}^{n+1} = 0 \quad \text{in } \Omega \tag{10}$$

$$\mathbf{u}^{n+1} \cdot \tilde{\boldsymbol{\tau}}_\xi = \mathbf{u}^* \cdot \tilde{\boldsymbol{\tau}}_\xi \quad \text{on } \partial\Omega, \tag{11}$$

where $\partial\Omega = \partial\Omega_E + \partial\Omega_O$ and $\tilde{\boldsymbol{\tau}}_\xi$ is the unit vector tangent to the ξ-direction. Note that the pressure correction step is in itself a set of inviscid equations and is thus well posed only if the boundary condition on the normal velocity component is imposed. Equations (9) and (10) together give a Poisson equation for pressure which is solved and the pressure correction is added to the intermediate velocity $\mathbf{u}^*$, viz.,

$$\nabla^2 P^{n+1} = \frac{\nabla \cdot \mathbf{u}^*}{\Delta t} \quad \text{in } \Omega \tag{12}$$

$$\mathbf{u}^{n+1} = \mathbf{u}^* - \Delta t \nabla P^{n+1} \quad \text{in } \Omega + \partial\Omega. \tag{13}$$

Thus the pressure step can be viewed as the projection of the velocity field onto the divergence-free space.

To avoid severe viscous stability limits, all the terms in the wall-normal (ξ) diffusion term except the cross terms are treated implicitly using a Crank–Nicolson scheme. All non-linear advection terms, wall-tangential (η and z) viscous terms, and the cross-terms in the wall-normal diffusion term are treated explicitly using a third-order Adams–Bashforth scheme. In contrast to the second-order

Adams–Bashforth scheme, this scheme ensures stability in the limiting case of pure advection.

The potential flow is specified as the initial condition for the flow computations. Thus, the initial flow field is divergence free, a necessary condition for well posedness of the equations. For the non-zero angle-of-attack case, no artificial perturbation is needed to initiate vortex shedding and, by specifying the initial condition as potential flow, conditions for the startup process are simulated accurately. For the case of zero angle-of-attack, an artificial perturbation is needed to break the symmetry about the x-axis and initiate the shedding process. Furthermore, for the 3D simulations, a spanwise perturbation is also needed in order for the flow to develop three-dimensionality. Two desirable properties of any such artificial perturbation are that it should neither introduce any divergence nor any net circulation. For breaking the symmetry about the x axis, we impose a slip velocity on the surface of the cylinder sinusoidally (a conveyor-belt type mechanism) for a short period of time. For the spanwise perturbations, a small random spanwise variation is given to the slip velocity at the cylinder for a short period of time and the three-dimensionality is allowed to develop on its own subsequently.

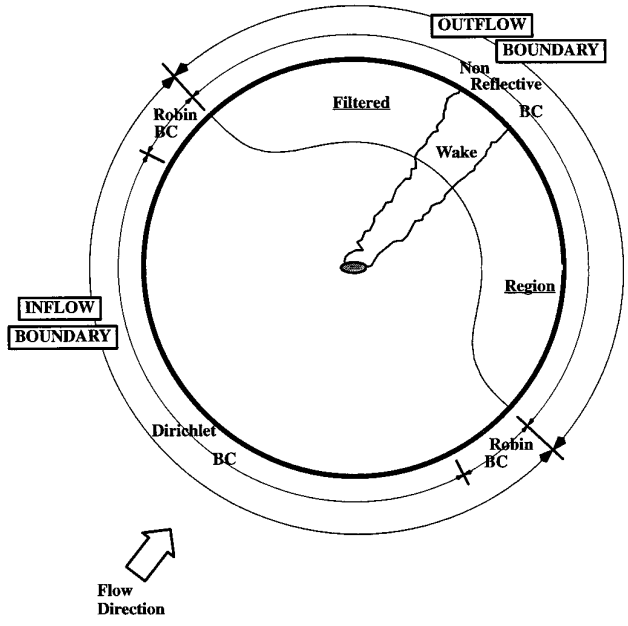

FIG. 2. Schematic of the computational domain showing the various boundary conditions at the outer boundary.

Boundary Conditions

Application of appropriate and well posed boundary conditions at the cylinder surface and at the outer boundary is crucial for the present simulations. The inflow and outflow boundary conditions are applied on different sections of the computational boundary as shown in Fig. 2. Details of the various boundary conditions are given in the following sections.

Inflow Boundary Condition

The most straightforward inflow boundary condition is the Dirichlet boundary condition specifying the inflow as the potential flow. This follows from the reasonable assumption that far upstream of the body, the displacement effect of the body is negligible and thus the flow is very close to potential flow. In reality, the behavior at the outer boundary becomes clear if one considers the perturbation velocity (where ''perturbation'' refers to the perturbation from potential flow). The momentum defect in the wake appears as an inflow in the perturbation velocity which is balanced by an outflow over the rest of the outer boundary. This perturbation outflow is maximum in the region directly above and below the body and reduces in the upstream region. Furthermore, due to the displacement effect the flow encounters a body which is more bluff than the actual shape and, thus, it tends to accelerate more than the potential flow as it goes over the body. By imposing the potential flow as the Dirichlet boundary condition at the inflow, the displacement effects are not allowed at the inflow part of the outer boundary whereas at the outflow part, where a convective boundary condition is imposed, the flow is able to adjust to the presence of the body. This leads to a sharp variation of velocity at the junction of the inflow and outflow sections of the outer boundary. This discontinuity, although fairly small in magnitude compared to the potential velocity, is enough to generate oscillations associated with the Gibbs phenomenon and its effect is felt throughout the computational domain due to the global nature of the computations.

Thus, there is a need to devise an inflow boundary condition which will smooth out the discontinuity in the vicinity of the inflow–outflow junction. The boundary condition should allow for the flow to react to the blockage effect of the cylinder. Also we require the Dirichlet boundary condition over most of the inflow boundary so as to maintain control on the incoming flow. With these constraints in mind, the following mixed boundary condition is used at the inflow boundary

$$B(\mathbf{u}^*) = \mathbf{u} - \mathbf{u}_{\text{in}} + \varepsilon(\eta)\left(\frac{\partial \mathbf{u}}{\partial \xi} - \frac{\partial \mathbf{u}_{\text{pot}}}{\partial \xi}\right) = 0 \quad \text{on } \partial\Omega_{\text{in}}, \quad (14)$$

where $\partial\Omega_{\text{in}}$ is the inflow part of the outer boundary; $\varepsilon(\eta)$ is the coefficient of the Neumann part and is a function that varies smoothly from a value of zero in the upstream region to a small value ($\sim$0.1) at the inflow–outflow junction. Thus, since the coefficient of the Neumann part is

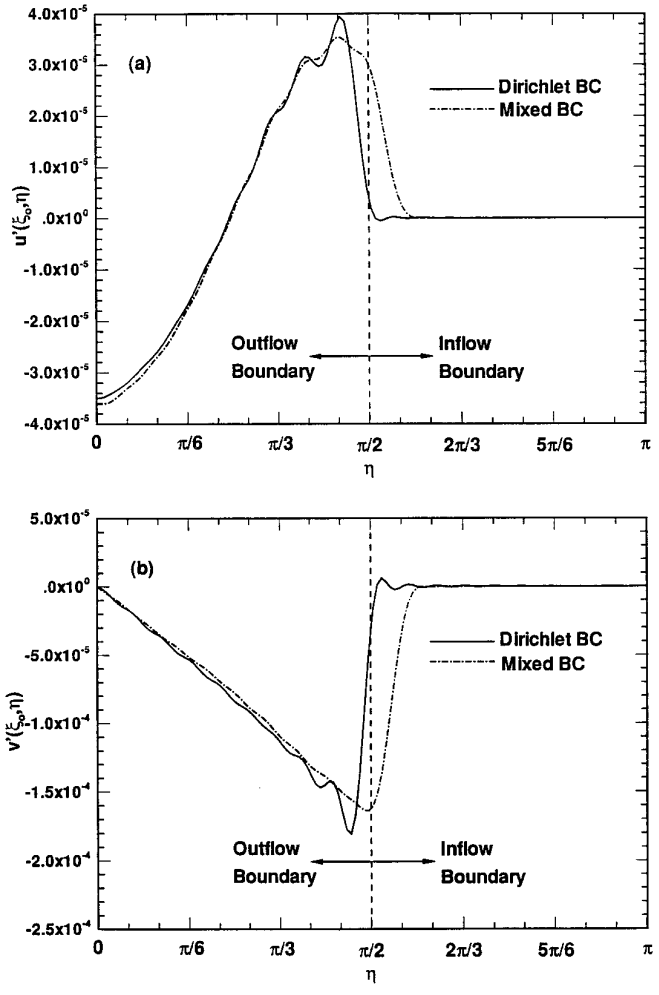

FIG. 3. Comparison of perturbation velocities obtained at the outer boundary with Dirichlet and mixed inflow boundary conditions. ($\mathscr{I} = 0.5$, $\alpha = 0°$, Re = 1000): (a) u' variation at the outer boundary. (b) v' variation at the outer boundary. Both figures show that the mixed boundary condition reduces the Gibbs phenomena at the inflow-outflow junction.

small, the above boundary condition is primarily a Dirichlet boundary condition. The small Neumann part is, however, crucial in that it allows the flow some freedom in the vicinity of the inflow–outflow junction; $\mathbf{u}_{\text{in}}$ is the Dirichlet part of the inflow boundary condition and is specified as

$$\mathbf{u}_{\text{in}} = \mathbf{u}_{\text{pot}} + \Delta t(2\nabla P^n - \nabla P^{n-1}). \tag{15}$$

The above boundary condition, coupled with a homogeneous Neumann pressure boundary condition, ensures that in the strictly Dirichlet portion of the inflow boundary the normal velocity is exactly equal to the potential value and the tangential components are equal to the corresponding potential values up to $O(\Delta t^3)$ [22].

In Fig. 3a we compare u' (which is equal to $u - u_{\text{pot}}$) at the outer boundary, obtained with the two different inflow boundary conditions, and Fig. 3b shows the corresponding v' distribution. The result shown is for a simulation with $\mathscr{I} = 0.5, \alpha = 0°$, and Re = 1000. Both figures show that the simulation using Dirichlet boundary conditions suffers from the Gibbs phenomenon whereas the mixed boundary condition shows negligible spurious oscillations. It should be noted that this is at an early stage in the simulation ($t = 2.5$) and the values of the perturbation are themselves small. However, the fact that the Gibbs phenomenon is apparent so early shows just how much damage a badly posed boundary condition can do. With the mixed boundary condition, the displacement effect due to the body is allowed to propagate upstream, thereby adjusting the flow and resulting in a well-behaved solution.

Outflow Boundary Condition

In the present simulations, the semi-infinite domain is truncated to a large but finite computational domain. The critical aspect of implementing this technique is the boundary condition at the outflow boundary. In the context of finite-difference simulations of compressible flow over circular cylinders, simple outflow boundary conditions based on primitive variables result in spurious secondary frequencies [23]. Such boundary conditions are catastrophic in spectral simulations due to their extreme sensitivity and only carefully derived characteristic variable boundary conditions produce stable and consistent results [23, 24].

For spectral simulations of incompressible flows, nonreflective boundary conditions have been proposed and successfully employed in conjunction with domain truncation. Notable among these are the buffer-domain [11] and viscous-sponge [1] techniques. These techniques recognize the fact that the source of possible reflections from the outflow boundary is in the elliptic nature of the governing equation arising from the viscous terms and the pressure field. The idea is to effectively remove this ellipticity at the outflow boundary. Here we have implemented this technique on a single domain where the first source of ellipticity is removed by carefully identifying the normal (ξ) diffusion terms in the momentum equations and smoothly attenuating them to zero at the outer boundary. Similarly, the ability of the pressure field to carry signals back into the domain from the outer boundary is nullified by attenuating the source term in the pressure Poisson equation near the outflow boundary. It should be pointed out that the technique of Street and Macaraeg [11] is intimately coupled with the use of separate regular and buffer domains which, they emphasize, is crucial in the context of spectral simulations. Similar consideration applies to the viscous-sponge technique [1] which is applied in conjunction with a spectral element method. Here this technique has been applied for a single domain spectral method and

this requires additional care in the implementation of the technique.

In the present solver, the attenuation of the normal diffusion and pressure source terms is carried out by multiplying the requisite terms by a ''filter function'' of the form

$$f(\xi, \eta) = 1 - \exp\left\{-\gamma\left[\left(\frac{\xi - \xi_O}{\xi_E - \xi_O}\right)^{\beta_1} + \left(\frac{\eta - \eta_\alpha}{\pi}\right)^{\beta_2}\right]\right\}, \tag{16}$$

where $\xi_E \le \xi \le \xi_O$ and $\eta_\alpha \le \eta \le \eta_\alpha + \pi$, η_α being the η location which lies along the angle-of-attack line. The above function is reflected about the line of angle-of-attack to get its representation in the other half of the domain. We choose to define the region where $f < 0.99$ as the ''filtered region'' (see Fig. 2), where the attenuation of the normal viscous and the pressure source terms is significant. The rest of the region (where $f \ge 0.99$) will be referred to as the unfiltered region. In addition to this, we also define the region, where $f < 0.01$, as the ''parabolized region'' where the filter attenuates the requisite terms to 1% of their reference levels and the equations can be considered parabolic. It should be stressed that there is no discontinuity in the filter at $f = 0.99$ or 0.01 and it varies smoothly and continuously in the whole domain. The shape and smoothness of the filter function and the extent of the filtered and parabolized regions can be controlled through the parameters γ, β_1, and β_2.

The function should be smooth; i.e., its spectra (both Chebyshev and Fourier) should show adequate decay. $\partial f/\partial \xi$ should numerically evaluate to zero close to the body in order to avoid spurious generation of vorticity. In particular, piecewise-defined filter functions, which work well in conjunction with multidomain computations [11], are definitely not compatible with the present single-domain simulations. Filtering should be limited to the outflow region and no filtering should be applied in the inflow region of the outer boundary. The region upstream of the cylinder adjusts to the presence of the cylinder only through the action of diffusion and pressure. Filtering the normal viscous and pressure source terms reduces the ability of the upstream flow to adjust to the displacement effect of the cylinder and leads to the development of a spurious boundary layer on the inflow region of the outer boundary. Finally, vortices get distorted in the parabolized region mainly due to the filtering of the pressure source term and this can lead to spurious generation of vorticity in the computational domain following the exit of the vortices. Thus, the extent of the parabolized region should be kept small in order to minimize spurious generation of vorticity.

The advection-diffusion equation is thus explicitly parabolized in the wake region at the outer boundary. Outside the wake region, the diffusive effects are negligible and the flow is primarily convective in nature. Thus, flow at the entire outflow boundary can be treated as being purely convective in the direction normal to the boundary and convective boundary conditions can be employed without the generation of any spurious boundary layer. Finally, the exact form of the advection diffusion equation (Eq. 6) is

$$f(\xi, \eta)\frac{\partial^2 \mathbf{u}^*}{\partial \xi^2} + \mathbf{F}(\xi, \eta)\mathbf{u}^* - \frac{2\,\mathrm{Re}}{\Delta t} h^2 \mathbf{u}^* = \mathbf{R}(\mathbf{u}^n) \quad \text{in } \Omega, \tag{17}$$

where the first two terms on the LHS are the normal diffusion terms that are treated implicitly ($\mathbf{F}(\xi, \eta)$ being the variable coefficient of the $\mathbf{u}^*$ term) and $\mathbf{R}$ consists of all the terms treated explicitly. In the wake region of the outer boundary, the above equation is purely convective, since $f = 0$ in that region. The convective boundary condition in (8) is then given by

$$\mathbf{B}(\mathbf{u}^*) = \mathbf{u}^* - \frac{\mathbf{R}(\mathbf{u}^n)}{\left[\mathbf{F}(\xi, \eta) - \dfrac{2\mathrm{Re}}{\Delta t} h^2\right]} = 0 \quad \text{on } \partial\Omega_{\text{out}}, \tag{18}$$

where $\partial\Omega_{\text{out}}$ is the outflow portion of the outer boundary. Furthermore, after incorporating the filter function, the final form of the pressure Poisson equation is given by

$$\frac{1}{h^2}\left\{\frac{\partial^2 P^{n+1}}{\partial \xi^2} + \frac{\partial^2 P^{n+1}}{\partial \xi^2}\right\} + \frac{\partial^2 P^{n+1}}{\partial z^2} = f(\xi, \eta)\frac{\nabla \cdot \mathbf{u}^*}{\Delta t} \quad \text{in } \Omega. \tag{19}$$

Equations (11) and (13) together result in the boundary condition for pressure

$$\nabla P^{n+1} \cdot \tilde{\tau}_\xi = 0 \quad \text{on } \partial\Omega_O \tag{20}$$

which is enforced over the entire outer boundary. It should be noted that alteration of the pressure Poisson equation leads to non-zero divergences in the filtered region and thus amounts to the introduction of artificial compressibility. Also, with the viscous filter, the momentum equation can be viewed as a variable viscosity problem and, therefore, applying the divergence-free condition on the momentum equation will not lead to a typical pressure Poisson equation. The time-split method then provides the most straightforward way of decoupling pressure from the momentum equation.

Street and Macaraeg [11] suggest linearizing the convection term about the potential flow in the buffer domain. This helps to ensure that the characteristics at the outflow boundary are strictly in the outgoing direction. However,

convecting disturbances out of the computational domain at the potential velocity, instead of the actual velocity, results in an increased mass imbalance between the net inflow and the net outflow. For the present simulation, the outflow boundary is sufficiently downstream of the body and it is unlikely that, even in the wake, the flow at the outflow boundary will ever reverse direction. Therefore, we choose not to linearize the convection term; however, we do check to make sure that the condition of strict outflow at the outflow boundary is never violated.

Boundary Conditions on the Body

In order to guarantee no penetration at the end of the full time step, the boundary condition for pressure on the surface of the elliptic cylinder is given by the Neumann boundary condition

$$\nabla P^{n+1} \cdot \tilde{\tau}_\xi = 0 \quad \text{on } \partial\Omega_E \tag{21}$$

and the corresponding intermediate velocity boundary condition is given by

$$\mathbf{u}^* = \Delta t(2\nabla P^n - \nabla P^{n-1}) \quad \text{on } \partial\Omega_E. \tag{22}$$

It should be noted since the tangential gradients of pressure on the cylinder are not specified, this results in a finite but small slip velocity of $O(\Delta t^3)$ [22].

The splitting errors and the resulting numerical boundary layer that develops close to the no-slip boundary have been analyzed in detail and higher-order methods and improved pressure and intermediate velocity boundary conditions to reduce these errors have been suggested [14–17]. The time-split method with the above boundary conditions (Eqs. (21) and (22)) has been used in the past to simulate a number of different types of flows, including Taylor–Couette flow [22] and turbulent square duct flow [25], and has led to satisfactory results. However, in the present simulations, Eq. (21) may be a poor approximation, especially at the stagnation, separation, and reattachment points. Also in separated flows, the initial roll up and vortex shedding processes may be influenced by the non-zero slip velocity on the body. To test the performance of the above boundary conditions we employed an alternate formulation of the time-split scheme where both the no-slip and the correct pressure boundary condition were satisfied exactly. Following Marcus [21], an influence-matrix technique was implemented in conjunction with the time-split method. This implementation differs from the Kleiser and Schumann [20] influence-matrix technique which avoids all time-split errors. The current implementation of the influence-matrix technique, which is done in conjunction with the time-split scheme, basically adjusts the intermediate wall-normal and tangential velocity components such that, at the end of the pressure correction step, no-slip and no-penetration conditions are satisfied exactly and the pressure satisfies the wall-normal momentum equation as follows:

$$\mathbf{u}^{n+1} = 0, \quad \nabla P^{n+1} \cdot \tilde{\tau}_\xi = \frac{1}{\mathrm{Re}} \nabla^2 \mathbf{u}^{n+1} \cdot \tilde{\tau}_\xi \quad \text{on } \partial\Omega_E. \tag{23}$$

Thus, the boundary conditions are consistent with those of the full Navier–Stokes equations. Details of the formulation of this technique are given in the Appendix.

A number of 2D simulations have been performed with the two different surface boundary conditions and the results compared. No difference in the flow field and quantities including lift and drag coefficients and Strouhal numbers have been observed. A closer look at surface pressure and vorticity also shows no significant differences. This clearly shows that the time-split procedure and the boundary conditions (21) and (22) work satisfactorily even in the simulation of bluff body wakes which involve separation. Moreover, even though the influence-matrix method does not seem to gain much for the present simulations, it represents a methodology which might prove to be an attractive alternative for flows, where conventional coupled methods are difficult to apply (like variable viscosity problems) and where splitting errors introduced by ad-hoc boundary conditions may be unacceptable (like boundary driven flows).

Solution Algorithm

The overall solution procedure consists of two steps. The first step is the advection-diffusion step, where the discretized version of Eq. (17) is solved to obtain the intermediate velocity $\mathbf{u}^*$. Due to the explicit discretization of the advection-diffusion equation along the η and z directions, Eq. (17) is simply a set of uncoupled ordinary differential equations in ξ for various η and z locations. Since at any given η location, $\mathbf{F}$ is a function of ξ only, Eq. (17) is a set of variable coefficient 1D Helmholtz equations which can be solved easily by computing the inverse of the discretized operators. Since the operators are independent of z, there are only as many operators as there are η points and, thus, storage of their inverses is not memory intensive.

To satisfy incompressibility exactly at the end of each time-step, the pressure Poisson equation must be solved in a fully implicit manner. This is computationally the expensive step and, therefore, efficient solution of the three-dimensional pressure Poisson equation is the key issue. One approach is to use iterative schemes such as GMRES or multigrid methods. The other approach is the direct method, where the operator is inverted without resorting to iterative schemes. Here we have developed an efficient direct solver for the 3D Poisson equation in elliptic cylin-

drical coordinates. The orthogonal curvilinear elliptic cylindrical coordinate system introduces a non-separable variable coefficient into the Poisson equations,

$$\frac{\partial^2 P}{\partial \xi^2} + \frac{\partial^2 P}{\partial \eta^2} + a^2(\sinh^2 \xi + \sin^2 \eta)\frac{\partial^2 P}{\partial z^2} = G(\xi, \eta, z), \quad (24)$$

where $G(\eta, \eta, z)$ represents the source term of the pressure Poisson equation (Eq. 19) multiplied by h^2. In the context of a spectral simulation, the dependence of the coefficient on the azimuthal coordinate (η) hinders straightforward Fourier transform along this direction. However, the limited bandwidth of this variable coefficient can be exploited in developing an efficient direct solver. First the equation is Fourier transformed in the z direction in a straightforward manner. The next step is to transform the equation in the η direction. The transformed equation in Fourier space can be written as

$$\frac{\partial^2 \hat{P}|_{k_\eta}}{\partial \xi^2} - \left[k_\eta^2 + a^2\left(\sinh^2 \xi + \frac{1}{2}\right)k_z^2\right]\hat{P}|_{k_\eta} + a^2 k_z^2 \hat{P}|_{k_{\eta-2}} + a^2 k_z^2 \hat{P}|_{k_{\eta+2}} = \hat{G}|_{k_\eta}. \quad (25)$$

In the above equation, $\hat{P}$ and $\hat{G}$ now denote the transformed pressure and source terms, respectively, and k_z and k_η represent the wavenumbers in the spanwise and circumferential directions, respectively. Note that the dependence of the transformed variables on k_z is not explicitly shown. The above system of equations is uncoupled for the various Fourier modes in the z direction ($k_z = 0, \pm 2\pi/A, \pm 4\pi/A, ..., \pm N_z\pi/A$) and, therefore, each mode can be considered independently. Moreover, the odd and even modes in η are decoupled and two separate problems, one for the odd modes ($k_\eta = -N_\eta/2 + 1, -N_\eta/2 + 3, ..., N_\eta/2 - 1$) and one for the even modes ($k_\eta = -N_\eta/2 + 2, -N_\eta/2 + 4, ..., N_\eta/2$) can be solved separately. Let k_{O_j} denote the jth odd η-mode and k_{e_j} the jth even η-mode. Incorporating the Chebyshev collocation along the ξ-direction for each k_z mode, the fully discretized version of Eq. (25) for the odd η-modes becomes

$$[B]\hat{\mathbf{P}}|_{k_{o_{j-1}}} + [A_j]\hat{\mathbf{P}}|_{k_{o_j}} + [B]\hat{\mathbf{P}}|_{k_{o_{j+1}}} = \hat{\mathbf{G}}|_{k_{o_j}}. \quad (26)$$

In the above equation the matrix operators are given by $[A_j] \equiv [C] - k_{O_j}^2[I]$, $[B] \equiv a^2 k_z^2[I]$, and $[C] \equiv [D_{c2}] - [E]$. Here $[D_{c2}]$ is the Chebyshev collocation second derivative matrix, $[I]$ is the identity matrix, and the diagonal matrix $[E]$ is given by

$$[E]_{il} = \begin{cases} a^2(\sinh^2 \xi_i + \frac{1}{2})k_z^2 & \text{if } i = l \\ 0 & \text{otherwise,} \end{cases} \quad (27)$$

where ξ_i refers to the ith Chebyshev collocation location given by Eq. (5). Furthermore, $\hat{\mathbf{P}}$ and $\hat{\mathbf{G}}$ are vectors containing the values of $\hat{P}$ and $\hat{G}$ at the N_ξ collocation points, respectively, and all the above matrices are of size ($N_\xi \times N_\xi$). A similar linear system is also obtained for the even modes (k_{e_j}).

The linear system of equations represented by Eq. (26) is block tridiagonal with ($N_\eta/2$) $\times$ ($N_\eta/2$) blocks of size ($N_\xi \times N_\xi$) each and can be solved using the Thomas algorithm. A straightforwrad implementation of the Thomas algorithm requires the inverse of the individual blocks. As can be seen in Eq. (26), only the diagonal blocks are dense. The off-diagonal blocks are simply constant diagonal matrices and their inverse can be evaluated easily. A straightforward inversion and storage of the diagonal blocks accelerates the repeated solution of the linear system (Eq. 26) using the Thomas algorithm. However, this approach requires memory storage of the order of ($N_\xi^2 N_\eta N_z$) for the storage of the inverse, which for a typical 3D simulation would amount to hundreds of megabytes of memory. This memory requirement can be greatly reduced by exploiting the structure of the diagonal blocks $[A_j]$. For each spanwise wavenumber k_z, these diagonal blocks share a common ($N_\xi \times N_\xi$) matrix $[C]$ and differ only in their diagonal entries $k_{o_j}^2[I]$. Thus, the inverse of $[A_j]$ can be conveniently computed as

$$[A_j]^{-1} = [M]\left[[\lambda] - k_{o_j}[I]\right]^{-1}[M]^{-1}, \quad (28)$$

where $[M]$ is the eigenvector matrix of $[C]$, $[M]^{-1}$ is its inverse, and $[\lambda]$ is the corresponding diagonal eigenvalue matrix. With this approach, the storage requirement is reduced to ($N_\xi^2 N_z$).

Boundary conditions for the pressure can be easily incorporated within this formulation. Periodic boundary conditions along η and z are implicitly built into the Fourier expansion along these directions. Dirichlet boundary conditions in the ξ-direction can be built into the matrix representation by appropriately modifying the block-tridiagonal system. Neumann boundary conditions can be incorporated by using the reduced matrix technique and modifying $[A_j]$ and $\hat{\mathbf{G}}$ appropriately [26]. A detailed description of the solution algorithm can be found in Ref. [27].

TEST OF THE OUTFLOW BOUNDARY CONDITION

Extensive tests have been performed to study the performance of the outflow boundary condition and, also, to determine the effects of the viscous and pressure filters on the vortices as they convect downstream through the filtered region to the outflow boundary. Studying vortices which are part of a Karman vortex street is not appropriate

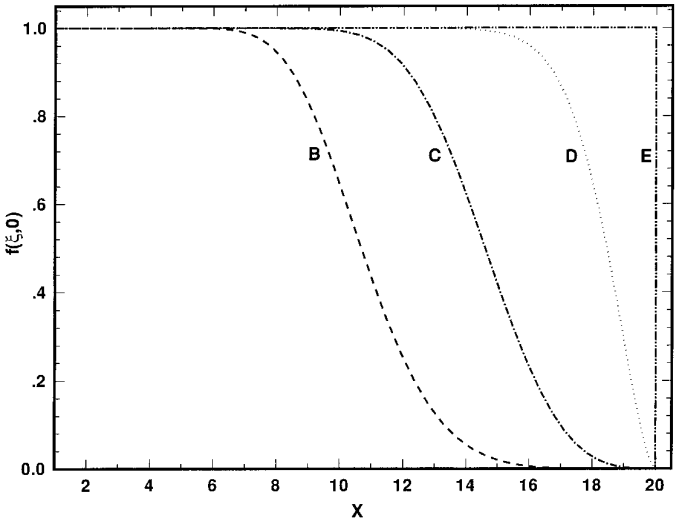

FIG. 4. Filter profile for all the filters used in the test of the outflow boundary condition. These profiles correspond to $f(\xi, 0)$, i.e., along the wake centerline.

for this purpose since the presence of many vortices which are being continuously shed and of the body which is constantly producing vorticity would make the results hard to interpret. Thus, a special simulation has been designed where a pair of vortices can be studied in isolation as they travel downstream. The simulation starts with the usual no-slip boundary conditions on the cylinder, mixed boundary conditions at the inflow, and non-reflective boundary conditions at the outflow boundary. These boundary conditions are maintained until the two vortices which were attached to the cylinder have grown to their full strength (which corresponds to $t = 12.5$). At this time, the no-slip boundary condition is replaced by potential velocities on the body. As a result, the two vortices detach from the cylinder and start convecting downstream. At the same time the strength of the vorticity layer on the cylinder starts to reduce and the flow begins to approach the potential flow.

The parameters chosen for this study are $\mathscr{T} = 0.5$, $\alpha = 0°$, and Re = 500, and a computational domain of size $x_O = 20$ is used. A number of filters with different extensions of the filtered region have been chosen to assess the effect of the filter on the flow field and the ability of the filter to convect large vortical disturbances out of the computational domain. Furthermore, a comparison of the performance of the various filters will allow us to choose the best filter for our purpose. The four filter shapes that have been chosen for this purpose are shown in Fig. 4. In addition to these four cases, we have also simulated the flow in a bigger domain (with $x_O = 30$), where the filtered region has been kept well outside $x = 20$. Thus, in this simulation the vortices convect downstream and out of the $x = 20$ region without encountering the filter. Therefore, this simulation leads to the base solution and the results of the other cases can be compared to this reference case to assess their performance. Finally, the effect of resolution on the performance of the filters is assessed by simulating one of the test cases with improved resolution. The various numerical parameters for all these cases are given in Table I. In the table, Case A corresponds to the reference case, Cases B–E are the four test cases, and Case F is the high resolution run which has the same filter as Case D.

A quantitative assessment of the performance of the outflow boundary condition can be made by computing the square integral of the spanwise vorticity (ω_z) given by $\|\omega_z\|_2^2 = \int_{\Omega_{20}} \omega_z^2 \, dx \, dy$, where Ω_{20} denotes the elliptic domain up to $x = 20$. This quantity is directly related to the energy spectra associated with the spanwise vorticity and is a good indicator of the deviation from the potential flow. Figure 5a shows the long time behavior of this quantity for all the six cases. First, we follow the evolution of $\|\omega_z\|_2^2$ for the reference case (shown by the solid line) in order to understand the behavior of the vortices as they convect downstream and exit Ω_{20} in the absence of any filtering. In the time interval $12.5 < t < 39$, the vortices move from near the body and arrive just upstream of $x = 20$. During this time, the strength of the vortices decays continuously due to viscous dissipation and this decay is apparent from the steady decrease in $\|\omega_z\|_2^2$ seen in Fig. 5a. At about $t = 39$, the downstream end of the vortices begins to exit and the vortices completely exit at around $t = 42$. During this period, as expected, there is a rapid drop in $\|\omega\|_2^2$. In Fig. 5b we zoom into the time interval $39 < t < 43$ so as to take a closer look at the behavior of this quantity as the vortices exit the computational domain.

The time evolution of $\|\omega\|_2^2$ for Case B follows that of the reference case until about $t = 33$. Thereafter, Case B deviates from the reference case and there is a more rapid decrease in this quantity and it reaches a minimum of about 0.5 at around $t = 41.4$ at which time the vortices completely

TABLE I

Domain and Filter Parameters Used in the Outflow Boundary Condition Test

Test case	N_ξ	N_η	Outer domain	Filtered region ($f(\xi, 0) < 0.99$)	Parabolized region ($f(\xi, 0) < 0.01$)	Attenuation factor
A	201	160	30	29	29.9	$\sim 10^4$
B	101	130	20	7	15.6	~ 20
C	101	130	20	10	18.6	~ 100
D	101	130	20	15	19.9	~ 1670
E	101	130	20	20	20.0	~ 70
F	151	160	20	15	19.9	~ 4000

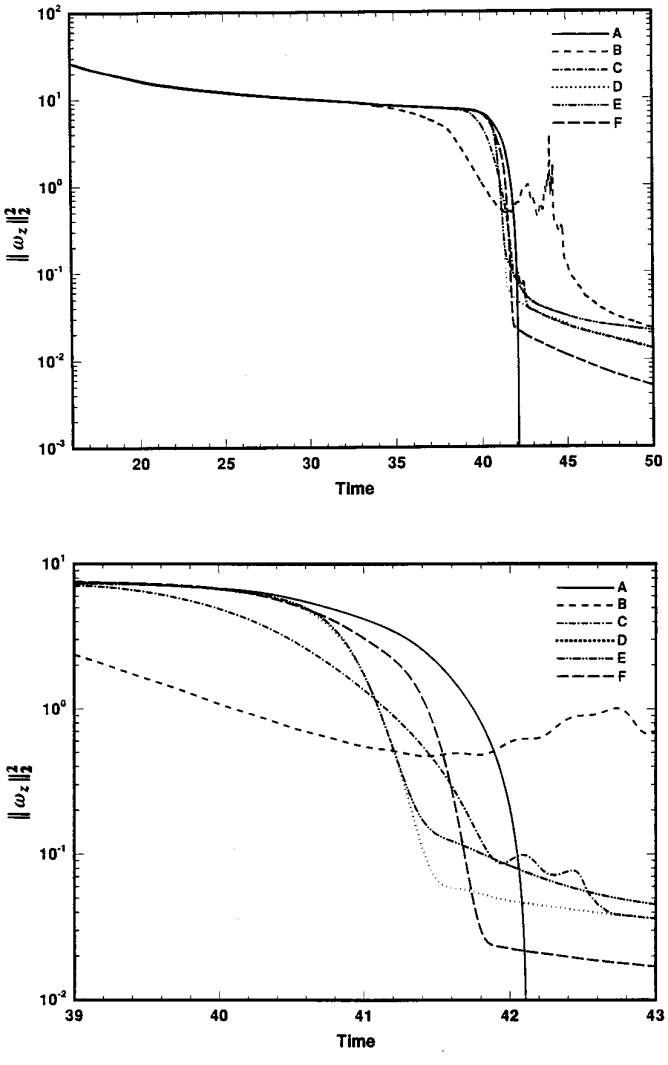

FIG. 5. Variation of square integral of spanwise vorticity with time for the various filters: (a) Long term behavior of the quantity as the vortices convect downstream from the vicinity of the body and convect out of the computational domain. (b) Close-up view of the variation of this quantity as the vortices approach the outflow boundary and convect out.

exit the domain. This suggests that the vortices undergo significant distortion due to the filter as they approach the outer boundary. In fact, at $t = 33$, the downstream end of the vortices has just entered the parabolized domain (where the filter has attenuated the normal viscous terms and the pressure source to about 1% of their reference levels). We observe that the distortion of the vortices is a result of the complete filtering of the pressure source term in the parabolized region. Subsequently, there is an increase in $\|\omega\|_2^2$ and it undergoes rapid and large variations before the final decay. These large variations are clear indications that the boundary condition is not able to adjust to the exiting vortices and this leads to the spurious increase of vorticity in the domain after the vortices have exited the domain.

In Case C, the filter is applied further downstream than in Case B with the filter extending from $x = 10$ to $x = 20$. However, as can be seen in Fig. 4, there is little difference in the shapes of the filters for Cases B and C. The main difference is in the extent of the parabolized region which is smaller for Case C (extending from $x = 18.6$ to $x = 20$). For this case, it is observed that the plot of $\|\omega\|_2^2$ coincides very well with that for the reference case until about $t = 38$ which corresponds to the time when the vortices have just entered the parabolized region. Thereafter, the curve departs from that of the reference case and reaches a local minimum of about 0.1 at $t = 42$ at which time the vortices have completely exited the outflow boundary. Subsequently, it undergoes some low level fluctuations due to the distortion of the vortices by the pressure filter in the parabolized region and the lower level of the fluctuations in this case is due to a smaller parabolized region.

Thus, the ability of the filter to allow for a smooth exit of the vortices from the computational domain depends very much on the extent of the parabolized region. Furthermore, contrary to expectations, a larger parabolized region does not necessarily imply a smoother exit of the vortices from the computational domain since pressure filtering leads to significant distortion of the vortices. However, the presence of a region where the pressure source term is completely filtered out is necessary since this ensures that the pressure disturbance that is created at the outflow boundary due to the exiting vortices does not affect the solution in the unfiltered region. This implies that there is an optimum filter (with an optimum size of the parabolized region) which will result in the maximum decay of vorticity as the vortices exit the computational domain and the objective then is to find this filter shape through numerical experimentation. Furthermore, so as to quantify the performance of the filters we introduce the ''attenuation factor'' which is the ratio of $\|\omega_z\|_2^2$ before the vortices exit the domain to just after they have exited the domain. The highest attenuation factor should be reached for the optimum filter. This quantity is also tabulated in Table I for the various test filters and a comparison of this quantity for Cases B and C clearly shows that filter C performs better than filter B.

In Case D, the filter is pushed further downstream and the parabolized domain now extends only between $19.9 < x < 20$. Figures 5a and 5b show that the plot of $\|\omega_z\|_2^2$ for this case departs from the reference case only after $t = 40$. Furthermore, the vortices exit the domain smoothly and no significant variation in $\|\omega_z\|_2^2$ is observed after the vortices have exited at around $t = 41.6$. The superior performance of this filter is also evident from the attenuation factor which is an order of magnitude larger than the previous cases.

Case E is a step filter (see Fig. 4), where the filter function takes a value of one everywhere except at the outflow boundary where it is zero. The $\|\omega_z\|_2^2$ curve for this case follows closely that of Case D, however, the attenuation factor achieved by this filter is significantly smaller than for Case D and is even smaller than Case C. This is a direct consequence of the absence of a parabolized region which allows pressure disturbances at the exit to reflect back into the computational domain. Furthermore, the large discontinuity in the filter function leads to Gibbs phenomenon at the outflow boundary and contributes to the decrease in the attenuation factor.

Thus, the filter in Case D seems to provide the best attenuation of vorticity and is the filter shape of choice. For this filter, the effect of improved resolution on the performance of the filter is investigated in Case F, where the resolutions in the wall-normal and circumferential directions are increased to $N_\xi = 151$ and $N_\eta = 160$. A noticeable improvement in the performance of the filter can be observed and an attenuation factor of about 4000 as compared to 1670 is obtained. Thus, part of the discrepancy between the reference case and the test cases is due to resolution. However, in actual simulations, filter C produces results which are virtually indistinguishable from those obtained using filter D. Thus, there is a range of filter shapes that perform equally well in actual wake simulations.

An issue of concern is the possible generation of spurious vorticity due to the introduction of the filter function into the governing equations. The error introduced in the vorticity equations is proportional to both $\partial f/\partial \xi$ and the magnitude of the viscous terms. This underscores the need for a smooth filter function and also requires that the filter be applied far enough downstream where the viscous terms are small. Proof that the spurious generation of vorticity is insignificant in the present simulations can be found in Fig. 5a. For Case C, the vortices enter the filter region around $t = 25$ and reach the parabolized region around $t = 38$. During this time, the vortices convect through a region of large streamwise gradient in the filter function ($\partial f/\partial \xi$) and should correspond to the largest generation of spurious vorticity. However, we notice in Fig. 5a that there is virtually no difference between this and the base case, implying no significant alteration of the vorticity distribution due to the filtering process.

Further evidence of the benign nature of the filtering process is obtained through detailed comparison of the shape and strength of the vortices as they convect through the filtered region and exit the outflow boundary. In Fig. 6 we have plotted a sequence of vorticity contour plots for the reference case (Case A) that show the vortices as they travel downstream and convect out of Ω_{20}. Only a slice of the computational domain has been extracted for plotting purposes and in all the plots, contours corresponding to

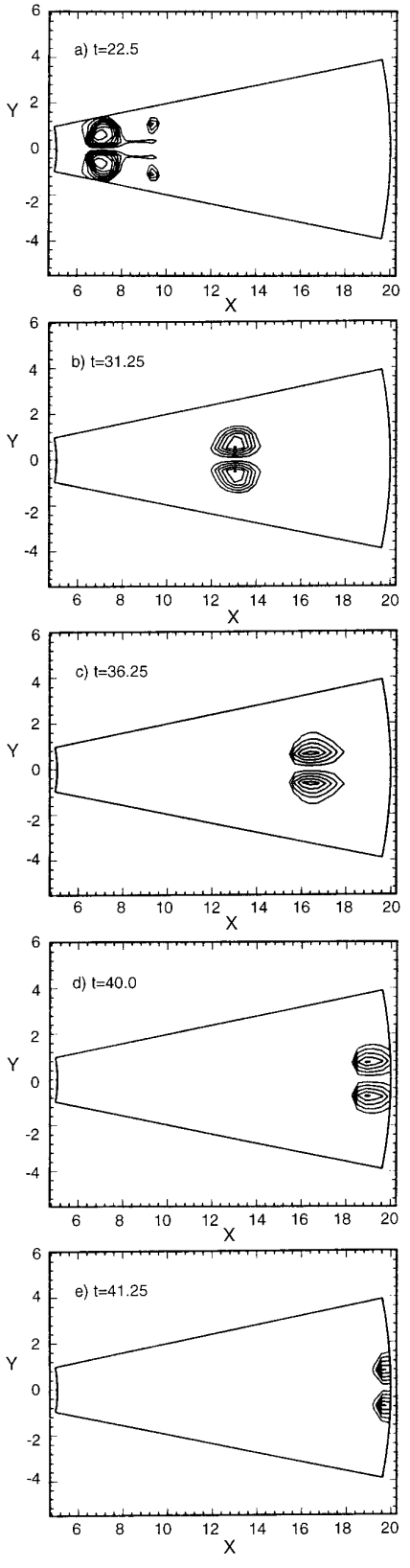

FIG. 6. Sequence of vorticity contours which show the two vortices as they convect downstream and out of Ω_{20} for the unfiltered reference case (Case A).

the same vorticity values (ranging between −2.6 and 2.6) have been plotted so that changes in the shape of the vortices can be followed. Figure 7 shows the corresponding plots for Case D.

Figures 6a and 7a show the vortices at $t = 22.5$, at which time the vortices are located at about $x = 7.0$. It can be observed that there is no noticeable difference in the structure of the vortices between the two cases. It should be pointed out that the two small vortices located downstream of the primary vortices result from the rollup of the shear layer as the vortices detach from the body and are, thus, artifacts of the startup process and the abrupt change in the boundary conditions at the body. Their presence should not affect the present study of the effectiveness of the outflow boundary condition. Figures 6b and 7b show the vortices at $t = 31.25$, at which time, for Case D, the vortices are just upstream of the filtered region. A comparison between the two cases reveals no significant difference in the structure of the vortices. Figures 6c and 7c correspond to a time when, for Case D, the vortices have entered the filtered region. As before, no differences are observed in the structure of the vortices for the two cases and this provides further evidence that filtering does not lead to the production of spurious vorticity. In the next two sets of figures, the vortices approach the outflow domain and exit the boundary at $x = 20$. In these plots, small differences in the structure of the vortices can be observed between the two cases; however, the vortices exit the outflow domain smoothly without any reflections. Here it should be stressed that differences between the filtered and unfiltered cases are unavoidable in the filtered region, even in the case of the best filter, since filtering alters the governing equations. The only requirement we need to impose is that the presence of the filter does not feed back and affect the region upstream of the filter and that, as the vortices exit the outer boundary, no spurious reflections are generated that affect the unfiltered upstream region.

Thus, the above tests allow us to determine the optimum filter shape for the present simulations. For the optimum filter (Case D), the tests show that the filtering procedure achieves its objective, in a satisfactory manner. Furthermore, it is established that the viscous filtering does not lead to the generation of spurious vorticity and the filtering process does not have any adverse effect on the flow in the unfiltered region. In addition to this, domain independence studies have also been performed, and it is found that the computed flow field is relatively insensitive to the size of the outer domain [27].

Simulation Results

A number of 2D and 3D simulations have been performed in order to validatae the code and the results for

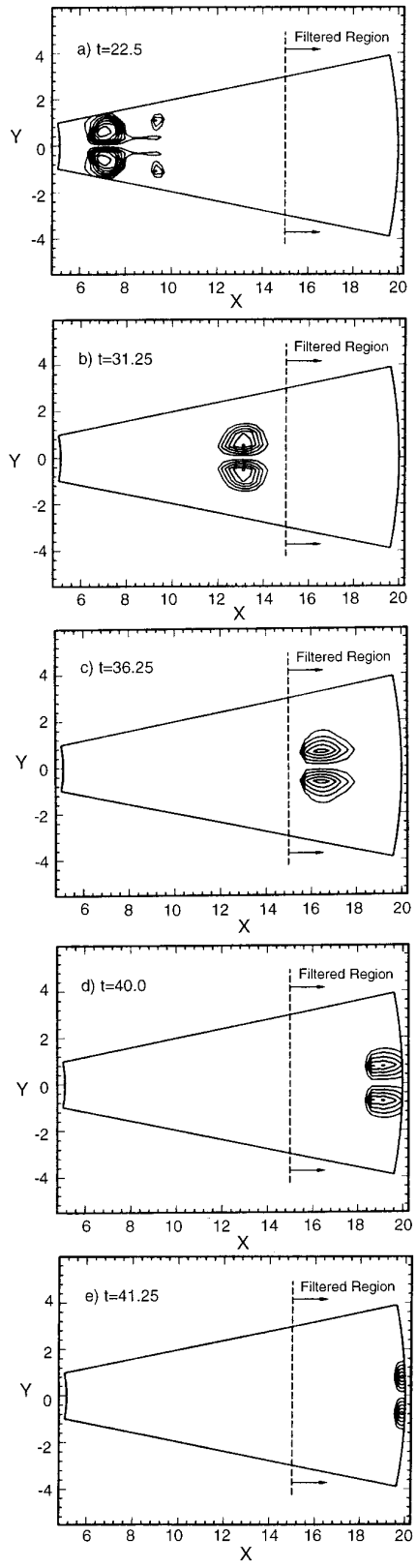

FIG. 7. Sequence of vorticity contours as the two vortices convect downstream and out of computational domain for Case D. Comparison with the corresponding plots in Fig. 6 shows that the filter has no noticeable effect on the vortices as they convect through the unfiltered region and the vortices exit the computational domain in a smooth manner.

TABLE II

Summary of the Various Cases That Have Been Simulated and Comparisons with Available Experimental Results

Case no.	Present simulations				Experimental results		
	Parameters	$N_\xi \times N_\eta \times N_z$	St*	$\overline{C}_D$	Parameters	St*	$\overline{C}_D$
1	$\mathscr{T} = 0.2$, $\alpha = 45°$, Re* = 163				$\mathscr{T} = 1.0$ $\alpha = 0°$, Re* = 163	0.18	—
	2D	81×100	0.19	3.71	Williamson (1988)		
2	$\mathscr{T} = 0.5$, $\alpha = 0°$, Re* = 1000				$\mathscr{T} = 1.0$, $\alpha = 0°$, Re* = 1000	0.21	—
	2D	81×100	0.20	0.61	Roshko (1954)		
3	$\mathscr{T} = 0.5$, $\alpha = 45°$, RE* = 525				$\mathscr{T} = 0.6$, $\alpha = 45°$, Re* = 10^4	0.23	—
	2D	81×100	0.24	2.52	Modi & Wiland (1970)		
	3D ($A = 2.0$)	$81 \times 100 \times 28$	—	1.81			
4	$\mathscr{T} = 1.0$, $\alpha = 0°$, Re* = 525				$\mathscr{T} = 1.0$, $\alpha = 0°$, Re* = 525	0.21	—
	2D	81×160	0.22	1.44	Roshko (1954)		
	3D ($A = 2.0$)	$81 \times 160 \times 40$	0.22	1.24	$\mathscr{T} = 1.0$, $\alpha = 0°$, Re* = 525	—	1.15
					Wieselsberger (1922)		
5	$\mathscr{T} = 0.5$, $\alpha = 0°$, Re* = 525				$\mathscr{T} = 1.0$, $\alpha = 0°$, Re* = 525	0.21	
	2D	81×160	0.21	0.78	Roshko (1954)		
	3D ($A = 2.0$)	$81 \times 160 \times 40$	0.24	0.77			

five different configurations are presented in Table II. For all these simulations the outer extent of the computational domain, x_O, is 30. A CFL number based on the convection term in elliptic coordinates is used as a guideline in choosing the time step. Simulations have shown that a stable time-stepping is achieved for CFL $\approx$0.15 which for the grids used corresponds to a Δt in the range 0.002–0.006 for the various simulations. The 3D simulations require about 6.5 μs per time step per grid point on a single-processor Cray C-90, which for a typical 3-D grid amounts to about three hours of CPU time for simulating one vortex shedding cycle. The 3D run is initiated by perturbing the fully developed 2D flow and about 10 shedding cycles are required for the flow to attain a fully developed 3D state. Thus, the total CPU time required for one such 3D simulation is between 50–60 h.

In spectral methodology, the adequacy of grid resolution is commonly investigated in terms of the spectral decay along the coordinate directions. Here we investigate the energy spectra of the u-component of velocity for the 3D simulation of Case 5. Figure 8a shows the azimuthal energy spectra averaged along the span obtained at an instant in time. Due to inhomogeneity along the ξ-direction, the azimuthal spectra is shown for three different locations in order to verify the η-resolution in the boundary layer, in the near wake, and at a sufficiently downstream location. From the figure it is clear that there are at least five orders of magnitude decay in the azimuthal energy spectra at all these locations. The radial resolution is investigated in Fig. 8b, where the Chebyshev spectra is plotted at three different η-locations in the wake. Here, too, at least five orders of magnitude decay in the energy spectra can be observed. Finally, Fig. 8c shows the spanwise energy spectra at three different points in the near wake, where the three-dimensional streamwise structures are most active. More than seven orders of magnitude in the spanwise energy spectra can be observed, indicating very good resolution along z. It should be emphasized that similar spectral decay is observed for other velocity components and pressure and at other time instances during the shedding cycle. Thus, the grid chosen for the simulations provides adequate resolution of the flow field.

In Table II, the Strouhal number and Reynolds number are based on the projected width, L^*, of the cylinder. Thus, St* and Re* are equal to $\mathscr{T}L^*/U_\infty$ and L^*U_∞/ν, respectively, where $\mathscr{T}$ is the oscillation frequency. St* is useful since it can be used for comparison between flows over elliptic cylinders of various thickness ratios and angles-of-attack at the same Re*. In particular, St* can be compared with the corresponding Strouhal number for flow over a circular cylinders in order to validate our results. Finally, the aerodynamic force coefficients are defined as $C_L = L/\frac{1}{2}\,\varrho U_\infty^2 2L_y L_z$ and $C_D = D/\frac{1}{2}\varrho U_\infty^2 2L_y L_z$, where L and D are the lift and drag forces on the cylinder, respectively, and ϱ is the density of the fluid.

Three-dimensional simulations have been performed for different configurations at a Reynolds number of 525. Flow over a circular cylinder has been observed to become three-dimensional beyond a Reynolds number of about 180 [1, 3], and we expect the flow around elliptic cylinders to

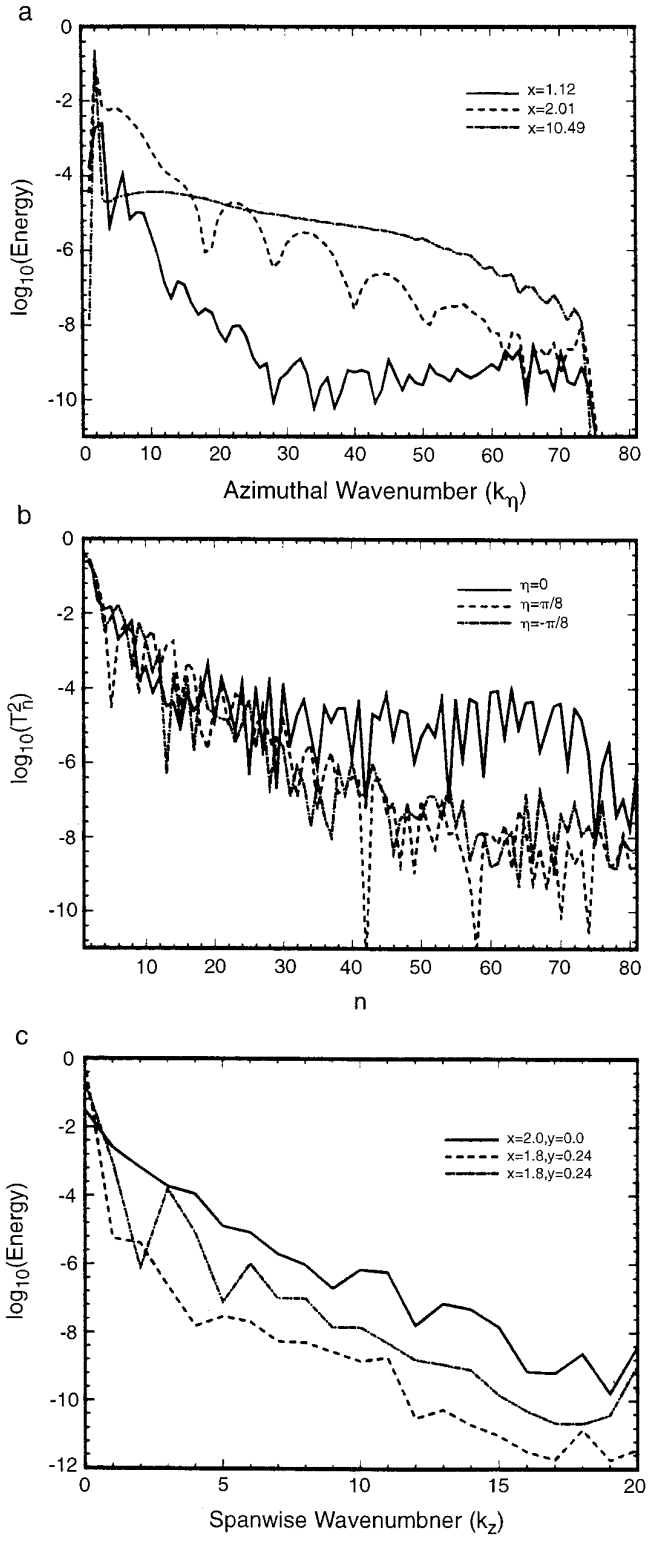

FIG. 8. Energy spectra of the u-velocity component along the three coordinate directions. At least five orders of magnitude decay is observed for all the directions.

behave qualitatively in a similar manner. Also, it has been observed experimentally that the spanwise wavelength of the streamwise structures in the wake of a circular cylinder in the Reynolds number range of 300 to 1000 is typically equal to one diameter [3, 28]. Thus, for the present 3D simulations, the spanwise length is adequate to capture at least one pair of streamwise structures. Visualization of the saturated 3D flow field has shown that there are in fact, one, two, and three pairs of streamwise vortices for Cases 3, 4, and 5, respectively [27].

In the absence of comprehensive experimental data for elliptic cylinders, the present results are in most cases compared against corresponding experimental data for circular cylinders. From Table II it can be observed that the present simulations predict the Strouhal number of vortex shedding with reasonable accuracy. It should be pointed out that at these relatively low Reynolds numbers no lower secondary frequencies are observed. Such secondary frequencies have been observed in other simulations [23] and are known to be caused by spurious reflections from the outflow boundary. The absence of these low frequencies in the current simulations further attests to the non-reflective nature of the outflow boundary conditions.

It is observed that 2D simulations, in general, predict a higher mean drag coefficient than the corresponding 3D simulations. Furthermore, for the case of a circular cylinder (Case 4), the drag computed from the 3D simulation compares better with the experimental value than the corresponding 2D simulation. The 2D drag coefficient values are 74%, 16%, and 1.3% higher than the corresponding 3D values for Cases 3, 4, and 5, respectively. Cases 3 and 5 correspond to flow over an elliptic cylinder of thickness-ratio of 0.5 at 0° and 45° angles-of-attack, respectively. Case 4 corresponds to a circular cylinder and all three simulations are at an identical Reynolds number of 525. Thus, it is evident that 2D simulations estimate the drag more accurately for streamlined bodies than for bluffer bodies. The underlying cause for the discrepancy in the mean drag has been studied in detail and it has been found that the overprediction of drag in 2D simulations is due to larger in-plane ($\xi - \eta$ plane) Reynolds stresses [31].

Figure 9 shows the variation of the lift and drag coefficients for Case 5 as the flow transitions from a fully developed two-dimensional flow to a saturated three-dimensional flow. The spanwise perturbation is provided at $t = 68$ and the three-dimensionality saturates at around $t = 102$. Although for this case there is no significant reduction in the average drag level, Fig. 9 shows that there is a considerable (48%) decrease in the peak-to-valley amplitude of the lift variation. A similar reduction is also observed for Cases 3 and 4. The underlying cause for this discrepancy in the lift fluctuation has been investigated in detail in Mittal and Balachandar [31] and it has been observed that the Karman vortices approach closer to the

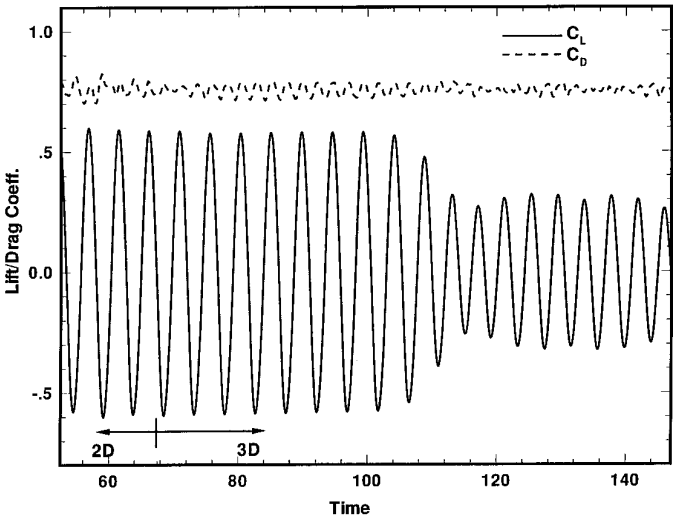

FIG. 9. Variation of lift and drag variation with time for Case 5 as the flows transition from a fully developed two-dimensional flow to a saturated three-dimensional flow. The spanwise perturbation is given at $t = 68$ and the three-dimensionality saturates at about $t = 102$.

cylinder base during shedding in 2D simulations than they do in 3D simulations and this leads to a higher lift amplitude level in 2D simulations.

CONCLUSIONS

The solver developed for the simulation of flow over elliptic cylinders is an efficient one in terms of both the CPU and memory requirement and will allow us to make a comprehensive analysis of the various aspects of the 3D flow field. The outflow boundary condition has been handled by parabolizing the governing equations near the outflow boundary and the issues in the implementation of this technique have been discussed in detail. Comprehensive tests have been carried out to assess the performance of this outflow boundary treatment. These tests have shown that with a carefully chosen filter function, large vortical disturbances are convected out of the computational domain without any spurious reflections. In addition to these tests, in actual wake simulations, we find that the vortex shedding process is relatively insensitive to the size of the outer boundary and no spurious secondary frequencies are observed in the present simulations at moderate Reynolds number where it is known from experiments that no such frequencies exist. This provides strong evidence that the outflow boundary condition performs satisfactorily in actual wake simulations. A novel inflow boundary condition has also been proposed that allows for the blockage effect of the body to be "felt" in the inflow portion of the outer computational boundary. It has been demonstrated that this boundary condition improves the overall behavior of the solution.

The use of the ad-hoc pressure and velocity boundary conditions in conjunction with the time-split method cannot be justified a priori for separated flows. An alternate formulation of the two-step time-split method which satisfies pressure and velocity boundary conditions that are consistent with the governing equations has been implemented. However, we observe that this does not lead to any significant difference in the flow including the surface pressure and vorticity distribution. Therefore, the conclusion is that the conventional time-split method with homogeneous Neumann pressure boundary conditions performs adequately for separated flows and predicts the flow field in a satisfactory manner. A number of 2D and 3D simulations have been performed and quantities like Strouhal numbers and drag coefficients show good agreement with established experimental results.

It is observed that three-dimensionality has a significant effect on the lift and drag forces of the cylinders; 2D numerical models at Reynolds numbers where the flow is known to be intrinsically three-dimensional, tend to overpredict both the average level of drag and the amplitude of lift fluctuations. In particular, it is observed that for flow past a circular cylinder, 3D simulations predict the mean drag more accurately than the corresponding 2D simulations. This has important implications in aero- and hydrodynamics where 2D simulations are used routinely as part of the design process.

APPENDIX: REMOVAL OF SPLITTING ERRORS FOR A TWO-STEP TIME-SPLIT SCHEME

A technique similar to the one used by Marcus [21] is used to impose the exact boundary conditions on the elliptic cylinder for a two-step time-split scheme. For the sake of simplicity, the discussion in this appendix will be restricted to two dimensions since extension to three dimensions involves no additional complications. Also, since this method is aimed towards improving the boundary conditions on the surface of the cylinder, boundary conditions at the outer boundary will be assumed to be known.

The influence-matrix technique reduces to identifying the correct wall-normal (α) and tangential velocity (β) boundary conditions which when enforced at the intermediate * level will result in no-slip and no penetration at the end of the full time-step with the additional condition that the pressure satisfy the normal momentum equation at the body. The equations and boundary conditions solved at the intermediate step can be written as

$$\mathcal{M}u^* = R_\xi \quad \text{in } \Omega; \quad u^*(\xi_E, \eta_j) = \alpha_j \quad \text{on } \partial\Omega_E \tag{29}$$

$$\mathcal{M}v^* = R_\eta \quad \text{in } \Omega; \quad v^*(\xi_E, \eta_j) = \beta_j \quad \text{on } \partial\Omega_E, \tag{30}$$

where $\mathcal{M}$ is the linear operator appearing on the LHS of

Eq. (17), R_ξ and R_η are the wall-normal and circumferential components of the right-hand side. Inflow and outflow conditions are enforced on $\partial\Omega_O$. This advection diffusion step is followed by the pressure correction step

$$\nabla^2 P^{n+1} = f(\xi, \eta)\frac{\nabla\cdot\mathbf{u}^*}{\Delta t} \quad \text{in } \Omega;$$

$$\nabla P^{n+1}(\xi_E, \eta_j)\cdot\tilde{\tau}_\xi = \frac{\alpha_j}{\Delta t} \quad \text{on } \partial\Omega_E \tag{31}$$

$$\mathbf{u}^{n+1} = \mathbf{u}^* - \Delta t\,\nabla P^{n+1} \quad \text{in } \Omega + \partial\Omega. \tag{32}$$

The Neumann boundary condition for the pressure Poisson equation, along with the pressure correction (Eq. 32), guarantee impermeability ($u^{n+1} = 0$) on the surface of the cylinder. As before, at the outer boundary $\nabla P^{n+1}\cdot\tilde{\tau}_\xi = 0$. Now α's and β's are to be chosen so that the resulting final velocity and pressure satisfy the no-slip condition and the wall-normal momentum equation at the body, given by

$$u^{n+1} = 0, \quad \nabla P^{n+1}\cdot\tilde{\tau}_\xi = \frac{1}{\mathrm{Re}}\nabla^2\mathbf{u}^{n+1}\cdot\tilde{\tau}_\xi \quad \text{on } \partial\Omega_E. \tag{33}$$

Let Eqs. (29)–(32) be called the ''A-problem.'' Since the functions α and β are unknown a priori in the calculation of u^* and v^*, the above A-problem cannot be solved directly. This difficulty can be avoided by using the influence matrix technique, where instead of solving the above A-problem, one solves for a particular solution (B-problem) and two sets of complementary functions (C-problem and D-problem). The particular solution (u_B, v_B, P_B) is obtained by solving Eqs. (29)–(32) with homogeneous boundary conditions $u^* = v^* = \nabla P^{n+1}\cdot\tilde{\tau}_\xi = 0$ applied on the cylinder. Each member of the first set of complimentary functions (u_C, v_C, P_C) is obtained as response to a unit source of intermediate wall-normal velocity placed at one point on the cylinder surface. Different members of the first set are thus built by placing the wall-normal velocity source at all the points on the cylinder surface one at a time. Thus, there are as many C-complimentary functions as there are numbers of points along the η directions, i.e., N_η. The equations solved for the jth C-problem then are

$$\mathscr{M}\,u^*_{C_j} = 0 \quad \text{in } \Omega; \quad u^*_{C_j}(\xi_E, \eta_l) = \delta_{jl} \quad \text{on } \partial\Omega_E \tag{34}$$

$$\mathscr{M}\,v^*_{C_j} = 0 \quad \text{in } \Omega; \quad v^*_{C_j}(\xi_E, \eta_l) = \delta_{jl} \quad \text{on } \partial\Omega_E \tag{35}$$

$$\nabla^2 P_{C_j} = f(\xi, \eta)\frac{\nabla\cdot\mathbf{u}^*_{C_j}}{\Delta t} \quad \text{in } \Omega;$$

$$\nabla P_{C_j}(\xi_E, \eta_l)\cdot\tilde{\tau}_\xi = \frac{\delta_{jl}}{\Delta t} \quad \text{on } \partial\Omega_E \tag{36}$$

$$\mathbf{u}^{n+1}_{C_j} = \mathbf{u}^*_{C_j} - \Delta t\,\nabla P_{C_j} \quad \text{in } \Omega + \partial\Omega. \tag{37}$$

Here the boundary conditions for the jth C-problem imply a unit wall normal velocity at the jth η-point and zero wall-normal velocity at all other wall points. A corresponding wall-normal pressure gradient is also enforced at this point to ensure zero penetration at the end of the full time step. The D-complementary functions can be obtained in a similar fashion where the solution of the jth D-problem will be obtained by applying a unit tangential slip at the jth η-point on the cylinder surface at the * level. The D-complementary functions satisfy no penetration at all the η-points automatically. The solution for the A-problem can then be written as a linear combination of the particular and complimentary solutions as

$$\begin{pmatrix} u^{n+1} \\ v^{n+1} \\ P^{n+1} \end{pmatrix} = \begin{pmatrix} u_B^{n+1} \\ v_B^{n+1} \\ P_B \end{pmatrix} + \alpha_j \begin{pmatrix} u_{Cj}^{n+1} \\ v_{C_j}^{n+1} \\ P_{C_j} \end{pmatrix} + \beta_j \begin{pmatrix} u_{D_j}^{n+1} \\ v_{D_j}^{n+1} \\ P_{D_j} \end{pmatrix}. \tag{38}$$

Here the unknown coefficients α's and β's are just the appropriate wall-normal and tangential velocity boundary values that will enable the overall velocity and pressure to satisfy Eq. (33). The algebraic relation for the α's and β's can be written in the following matrix form:

$$\begin{pmatrix} v_{C_j}^{n+1} & v_{D_j}^{n+1} \\ \tilde{\tau}_\xi\cdot\left(\nabla P_{C_j} - \dfrac{1}{\mathrm{Re}}\nabla^2\mathbf{u}_{C_j}^{n+1}\right) & \tilde{\tau}_\xi\cdot\left(\nabla P_{D_j} - \dfrac{1}{\mathrm{Re}}\nabla^2\mathbf{u}_{D_j}^{n+1}\right) \end{pmatrix}$$
$$\begin{pmatrix} \alpha_j \\ \beta_j \end{pmatrix} = \begin{pmatrix} -v_B^{n+1} \\ -\tilde{\tau}_\xi\cdot\left(\nabla P_B - \dfrac{1}{\mathrm{Re}}\nabla^2\mathbf{u}_B^{n+1}\right) \end{pmatrix}. \tag{39}$$

The vector on the RHS corresponds to the final slip error and normal momentum residual in the particular solution due to the imposition of ad-hoc homogeneous intermediate boundary conditions. The matrix on the left-hand side is the influence matrix, whose elements represent the slip error and normal momentum residual at every point on the body due to the placement of a unit penetration or slip source at a point on the surface. Solution of the above matrix equation provides the correct combination of complimentary functions that nullify the slip velocity and normal momentum residual produced at the cylinder by the particular solution. Thus the advection-diffusion and pressure correction steps in the A-problem become decoupled and the problem can be solved with the correct intermediate boundary conditions.

Once α's and β's are computed by solving Eq. (39), the final solution can be obtained in two different ways. The first option is to solve the A-problem with the correct intermediate boundary condition. Since the influence matrix can be computed once at the beginning and stored for repeated later use, the above option requires solving the momentum and pressure equation twice at each time step. The second option is to compute the final flow field using Eq. (38) which requires the storage of the two sets of complimentary functions, in addition to the influence matrix. In a general case, this option could be prohibitively expensive in terms of computer memory, even though this requires that the momentum equations be solved only once every time step. However, the present explicit formulation of the η and z viscous terms simplify the complimentary functions and reduce their required storage to order $(N_\xi N_\eta N_z)$, thereby allowing us to store them once at the beginning of the run. Thus, only the pressure Poisson equation needs to be computed again at each time step, leading to an increase of at most 40% in the CPU time. Therefore, it seems that there is a distinct advantage in treating the tangential viscous terms explicitly when combined with this influence matrix technique.

Finally, there are some subtle points which make the implementation of the current influence-matrix technique different from that of Marcus [21]. These differences arise due to the fact that his implementation is for a three-step time-split scheme whereas the current implementation is in conjunction with a two-step time-split scheme. The three-step scheme advances the solution sequentially through advection, pressure correction, and diffusion steps. For the three-step method, the intermediate velocity obtained after the pressure step satisfies the divergence-free condition. The final velocity after the diffusion step, however, satisfies the no-slip and no-penetration conditions exactly but is not divergence free. Therefore instead of no-slip, the divergence-free condition at the boundary is used to construct the influence matrix. In contrast to this, in the present formulation, requiring zero-boundary divergence of the final velocity leads to an ill-posed set of equations and results in explosive instability.

ACKNOWLEDGMENTS

These computations have been performed on the Cray-YMP at the National Center for Supercomputing Application at the University of Illinois at Urbana-Champaign and on the C-90 at the Pittsburg Supercomputing Center. Financial support for this work has been provided by the Schlumberger Technical Corporation under the Industrial Supercomputing Program Agreement. We also acknowledge the reviewers whose comments and suggestions led to improvement in the quality of the paper.

REFERENCES

1. G. E. Karniadakis and G. E. Triantafyllou, *J. Fluid. Mech.* **238,** 1 (1992).
2. A. Roshko, NACA Rep. 1191, 1954 (unpublished).
3. C. H. K. Williamson, *J. Fluid Mech.* **243,** 393 (1992).
4. I. Proudman and J. R. Pearson, *J. Fluid Mech.* **2,** 237 (1957).
5. H. Jafroudi, H-T. Yang, and J. Hermel, *J. Comput. Phys.* **109,** 289 (1993).
6. H. J. Lugt and H. J. Haussling, Naval Ship Research and Development Center Report 3748, Dept. of Navy, 1972 (unpublished).
7. H. J. Lugt and H. J. Haussling, *J. Fluid Mech.* **65**(4), 771 (1974).
8. K. E. J. Blodgett, M.S. thesis, Department of Aerospace Engineering and Engineering Mechanics, University of Cincinnati, 1989 (unpublished).
9. C. Canuto, M. Y. Hussaini, A. Quarteroni, and T. A. Zang, *Spectral Methods in Fluid Dynamics* (Springer-Verlag, New York, 1988).
10. A. T. Patera, *J. Comput. Phys.* **54,** 468 (1984).
11. C. L. Street, and M. Macaraeg, *Appl. Numer. Math.* **6,** 123 (1989).
12. N. N. Yanenko, *The Method of Fractional Steps for Solving Multi Dimensional Problems of Mathematical Physics in Several Variables,* edited by M. Holt (Springer-Verlag, Berlin, 1971).
13. A. J. Chorin, *Math. Comput.* **22,** 745 (1968).
14. S. A. Orszag, M. Israeli, and M. O. Deville, *Sci. Comput.* **1**(1), 75 (1986).
15. G. E. Karniadakis, M. Israeli, and S. A. Orszag, *J. Comput. Phys.* **97,** 414 (1991).
16. A. G. Tomboulides, M. Israeli, and G. E. Karniadakis, *J. Sci. Comput.* **4**(3), 291 (1989).
17. J. B. Perot, *J. Comput. Phys.* **108,** 51 (1993).
18. S. A. Orszag and L. C. Kells, *J. Fluid Mech.* **96**(1), 159 (1980).
19. J. Kim, and P. Moin, *J. Comput. Phys.* **59,** 308 (1985).
20. Klieser, L. and U. Schumann, ''Treatment of Incompressibility and Boundary Conditions in 3-D Numerical Spectral Simulations of Plane Channel Flows,'' in *Proceedings, 3rd GAMM Conf. on Numerical Methods in Fluid Mechanics, 1980,* edited by E. H. Hirschel, pp. 165–169.
21. P. S. Marcus, *J. Fluid Mech.* **146,** 45 (1984).
22. C. L. Street, and M. Y. Hussaini, *Appl. Numer. Math.* **7,** 41 (1991).
23. S. S. Abarbanel, W. S. Don, D. Gottlieb, D. H. Rudy, and J. C. Townsend, *J. Fluid Mech.* **225,** 557 (1991).
24. W. S. Don, and D. Gottlieb, NASA CR-182030, 1990 (unpublished).
25. R. K. Madabhushi, S. Balachandar, and S. P. Vanka, *J. Comput. Phys.* **105,** 199 (1993).
26. H. C. Ku, R. S. Hirsh, and T. D. Taylor, *J. Comput. Phys.* **70,** 439 (1987).
27. R. Mittal, Ph.D. thesis, Department of Theoretical and Applied Mechanics, University of Illinois at Urbana-Champaign, 1995 (unpublished).
28. H. Mansy, P-M. Yang, and D. R. Williams, *J. Fluid Mech.* **270,** 277 (1994).
29. V. J. Modi, and E. Wiland, *AIAA J.* **8**(10), 1814 (1970).
30. Wieselsberger, C., NACA TN 84, 1922 (unpublished).
31. R. Mittal, and S. Balachandar, *Phys. Fluids,* **7,** 1841 (1995).